UC San Diego
UC San Diego Previously Published Works

Title

Machine vision based detection of omega bends and reversals in C. elegans

Permalink

https://escholarship.org/uc/item/16n6g24b

Journal

Journal of Neuroscience Methods, 158(2)

ISSN

Authors

Huang, Kuang-Man
Cosman, Pamela
Schafer, William R

Publication Date

2006-12-01

DOI

Peer reviewed

Machine vision based detection of omega bends and reversals in *C. elegans*

Kuang-Man Huang [a],*, Pamela Cosman [a], William R. Schafer [b]

[a] *Department of Electrical and Computer Engineering, University of California at San Diego, La Jolla, CA 92093-0407, USA*
[b] *Division of Biological Sciences, University of California at San Diego, La Jolla, CA 92093-0349, USA*

Abstract

The behavior of the nematode *Caenorhabditis elegans* has proven increasingly useful for the genetic dissection of neurobiological signaling pathways and for investigating the neural and molecular basis of nervous system function. Locomotion is among the most complex aspects of *C. elegans* behavior, and involves a number of discrete motor activities such as omega bends (deep bends typically on the ventral side of the body which reorient the direction of forward locomotion) and reversals (changes in the direction of the locomotion wave that cause a switch from forward to backward crawling). Reliable methods for detecting and quantifying these movements are critical for escape reflexes and navigation behaviors. Here we describe a novel algorithm to automatically detect omega bends, which relies in part on a new method for obtaining a morphological skeleton describing the body posture of coiled worms. We also present an optimized algorithm to detect reversals, which showed improved performance over previously described methods. Together, these new algorithms have made it possible to reliably detect events that are time-consuming and laborious to detect by real-time observation or human video analysis. They have also made it possible to identify mutants with subtle behavioral abnormalities, such as those in which omega bends are dorsoventrally unbiased or uncorrelated with reversals. These methods should therefore facilitate quantitative analysis of a wide range of locomotion-related behaviors in this important neurobiological model organism.
© 2006 Elsevier B.V. All rights reserved.

Keywords: *Caenorhabditis elegans*; Classification; Coiler; Omega bends; Reversal; Skeleton

1. Introduction

The nematode *Caenorhabditis elegans* is widely used for studies of nervous system function and development. It has a simple nervous system which is well characterized at the anatomical level: an adult hermaphrodite contains only 302 neurons, each with a precisely determined position, cell lineage and synaptic connectivity. Despite its anatomical simplicity, the *C. elegans* nervous system mediates diverse and intricate patterns of behavior. It is well suited to analysis of the molecular and cellular basis of nervous system development and function. However, many genes with critical roles in the nervous system have effects on behavior that are difficult to describe precisely, or occur over time scales too long to be compatible with real-time scoring by a human observer. Automated systems (Baek et al., 2002; Cronin et al., 2005; Feng et al., 2004; Geng et al., 2004)

consisting of a tracking microscope and image processing software have been developed and used to follow and analyze the movements of individual animals at high magnification. Quantitative morphological and locomotion features can be obtained with this system and used to distinguish and classify the behavioral phenotypes of *C. elegans* mutants. For example, in Geng et al. (2003) the method was used to investigate the similarities between different behavioral patterns based on their clustering in multidimensional feature space.

In behavioral studies, it is often critical to parameterize a complex behavior by identifying the simpler behavioral events that underlie it. For example, among the most important behaviors to a nematode are those involving navigation of a sensory gradient to move toward an optimal condition; in chemotaxis behavior, this involves moving toward the highest concentration of a chemoattractant. Nematodes accomplish this navigation primarily using a movement called an omega bend, in which the animal makes a single deep body bend in a shape of the capital Greek letter omega, usually on the ventral side of the body (Croll and Smith, 1975; Croll and Smith, 1978; Pierce-Shimomura et

* Corresponding author. Tel.: +1 858 344 1816.
  E-mail address: houston21@hotmail.com (K.-M. Huang).

al., 1999). An omega bend serves to reorient the animal's head and allow it to continue to crawl forward, but in a different direction. An animal crawling down a chemoattractant gradient will tend to make frequent omega bends, which will reorient it up the gradient.

When avoiding noxious compounds, nematodes often exhibit a second form of behavior, known as an escape reflex. When a worm is touched or presented with a toxic chemical stimulus, it will switch the direction of the locomotion wave, causing the animal to instantaneously crawl backward instead of forward. After a short period of backward crawling, the animal will execute an omega bend and crawl forward in a different direction, away from the noxious stimulus. A variety of genes, including those encoding the *C. elegans* AMPA- and NMDA-type glutamate receptors (Zheng et al., 1999), affect the frequency of these reversals in direction. Moreover, the switch between forward runs and bouts of reversals has been shown to play an important role in worm touch avoidance behavior and is one of the key parameters affected by sensory cues (Wicks and Rankin, 1995). However, abnormalities in reversal frequency and particularly in reversal distance, are very difficult to detect by manual observation, and have only been verified by careful assays of individual animals (Rankin et al., 1990).

Efforts to understand the neural basis for complex locomotor behavior have begun to focus on the regulation of these simpler behavioral building blocks (Gray et al., 2005). In previous studies, reversals have been detected automatically by following the path of the animal's centroid and identifying a large change in the direction of bearing of the centroid trace (Hardaker et al., 2001). A more recent paper (Feng et al., 2004) described an algorithm that used skeleton points and the positions of the head and tail relative to the worm body to detect reversals. However, even the latter method sometimes fails to detect reversals accurately. Studies of omega bends have relied exclusively on the time-consuming analysis of video recordings by human observers. Detection of omega bends, whether by a human observer or a computer, requires a precise analysis of the animal's body posture during a turn. However, determining the correct posture using a standard morphological skeleton algorithm is challenging when the animal adopts a coiled posture or when the head touches the animal's body; in these cases, the normal skeletonizing algorithm does not correctly identify the true skeleton nor the correct ends of the worm (i.e. head and tail). Since animals frequently touch themselves during omega bends, detecting omega bends requires the development of an improved algorithm to define the biological skeleton of a coiled or touching body posture.

In this paper, we describe an algorithm which generates skeletons for coiled body positions. The algorithm uses a parameterized body model and locates the division line between overlapping portions of the worm body. Using this algorithm, we can robustly define the body postures of wild-type animals as well as of mutants that coil frequently. In addition, we have developed an algorithm based on skeleton analysis to detect omega bends and characterize parameters relevant to this behavior. In particular, the spatial polarity and temporal correlation of omega bends following reversals is investigated for wild type and several of the more active coiler mutants. We also develop an improved algorithm for detection of reversals.

In Section 2, we describe the skeleton algorithm, including image acquisition, pre-processing and its use in feature extraction and classification. We also describe our new algorithms for detecting omega bends and reversals. In Section 3, we present results assessing the robustness of our algorithms for defining coiler skeletons, omega bends and reversals. Discussion and conclusions appear in Section 4.

2. Materials and methods

2.1. Strains and culture methods

Routine culturing of *C. elegans* was performed as described (Brenner, 1974). All worms analyzed in these experiments were young adults (Fig. 1a); fourth-stage larvae were picked the evening before the experiment and tracked the following morning. Experimental animals were allowed to acclimate for 5 min before their behavior was analyzed. Plates for tracking experiments were prepared fresh the day of the experiment; a single drop of a saturated Luria broth (LB) culture of *E. coli* strain OP50 was spotted onto a fresh nematode growth medium (NGM) agar plate and allowed to dry for 30 min before use. The alleles and predicted products of the genes used in these experiments were as follows: *syd-1*(*ju82*); *unc-1*(*e1598*); *unc-3*(*e151*); *unc-10*(*e102*); *unc-17*(*e245*); *unc-26*(*m2*); *unc-32*(*e189*); *unc-37*(*e262*); *unc-75*(*e950*); *unc-77*(*e625*).

2.2. Acquisition of image data

C. elegans locomotion was tracked with a Zeiss Stemi 2000-C microscope mounted with a Cohu High Performance CCD video camera essentially as described (Geng et al., 2004). The microscope was outfitted for brightfield illumination from a 12 V 20 W halogen bulb reflected from a flat mirror positioned at an angle of approximately 45°. A computer-controlled tracker was used to maintain the worms in the center of the optical field of the microscope during observation. To record the locomotion of an animal, an image frame of the animal was captured every 0.125 s (8 Hz) for at least 5 min ($8 \times 60 \times 5 = 2400$ images per video). Next, we binarized the image using an adaptive threshold (the average value minus three times the S.D.) and found the connected component with the largest area. The original image was then trimmed to the smallest axis-aligned rectangle that contained this component, and saved as eight-bit grayscale data. The dimensions of each image, and the coordinates of the upper left corner of the rectangle box containing the worm body in the tracker field were also recorded simultaneously. The microscope was fixed to its largest magnification ($50\times$) during observation. The number of pixels per millimeter was fixed at 312.5 pixel/mm for all worms.

2.3. Image pre-processing

To facilitate analysis, the grayscale images were subjected to preliminary image processing to generate a simplified repre-
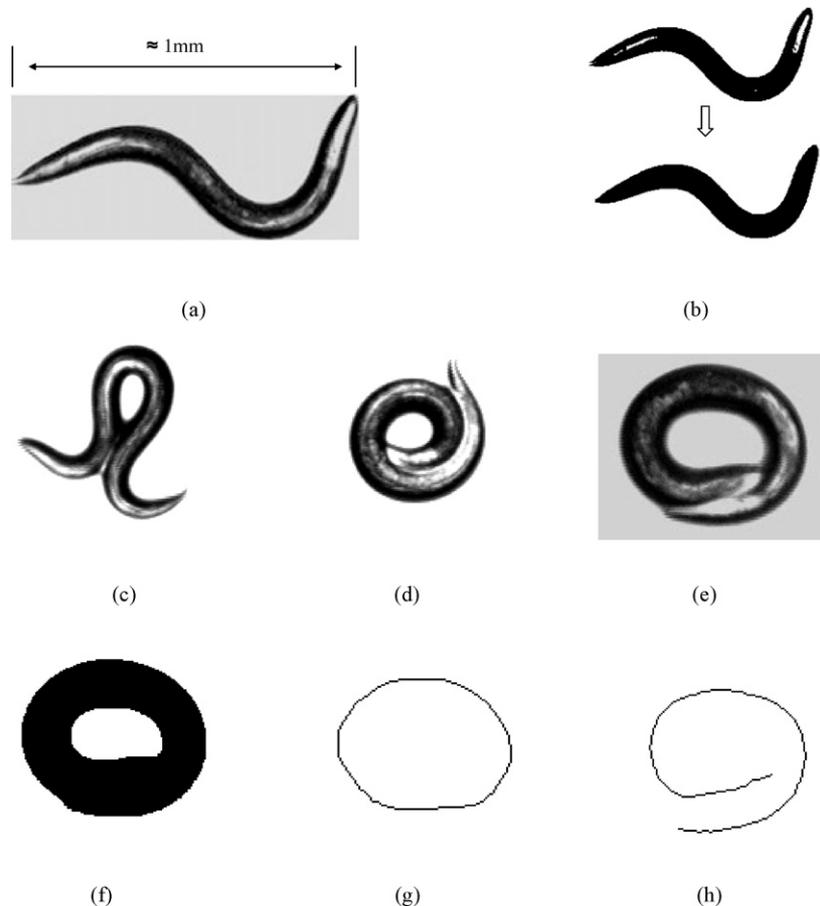
Fig. 1. (a) Example of a worm taking on a typical uncomplicated body posture (no touching or overlapping). (b) Hole-filling operator. (c) Typical omega bend. (d) Coil or spiral. (e) Grayscale image. (f) Binary image. (g) Skeleton from an image processing point of view. (h) Desired skeleton from a biological point of view.

sentation of the body (Geng et al., 2004). Briefly, an adaptive local thresholding algorithm followed by a morphological closing operator (binary dilation followed by erosion) was used. A corresponding reference binary image was also generated by filling holes inside a worm body based on image content information (Fig. 1b). The difference between these two binary images provided a good indication of which image areas are worm body and which are background. Following binarization, a morphological skeleton was obtained (Geng et al., 2004; Gonzalez and Woods, 2002; Jain et al., 1995).

2.4. Image feature extraction

Using the approach in Geng et al. (2004), the head and tail are recognized for entire video sequences using the brightness and the distance moved between the current frame and the previous frame for the two end points. Feature extraction is applied to obtain 64 basic features. These include body length, width, fatness, brightness and angle change rate. These 64 features are calculated for each of the 2400 frames in each video by using software coded in C. The maximum, minimum and mean values for most of these features were then computed to form 188 features in total for each video frame. Throughout this paper, we used the 90th and 10th percentile values as our maximum and minimum values for each feature in order to avoid extreme

values caused by noise or errors during image capture and processing. Certain features such as movement distance and speed could not be obtained from one single frame. In this case, we took 4, 8 and 40 frames (0.5, 1 and 5 s) in a sliding window and computed features within windows. The maximum, minimum and mean values were also calculated from these sets of numbers. A block diagram of system set-up is shown in Fig. 2.

2.5. Coiling skeletonizing

In most cases, the skeleton can be computed using a simple skeletonizing algorithm (Geng et al., 2004; Gonzalez and Woods, 2002). However, sometimes the binary worm body shape has an internal hole, which can be caused when the body bends into an omega shape (Fig. 1c) or a spiral (Fig. 1d). In such cases, the morphological skeleton which is correct from an image processing point of view is not necessarily a useful summary of the worm body shape from a biological point of view. For example, Fig. 1f shows the binarization of the worm body from Fig. 1e and g shows the morphological skeleton, correct from an image processing point of view, generated from the binary shape of Fig. 1f. Fig. 1h, on the other hand, shows the desired skeleton from a biological perspective. In previous studies, frames such as Fig. 1e could be recognized as failing the skeletonization (for example, because Fig. 1g skeleton is too short) and so the frame
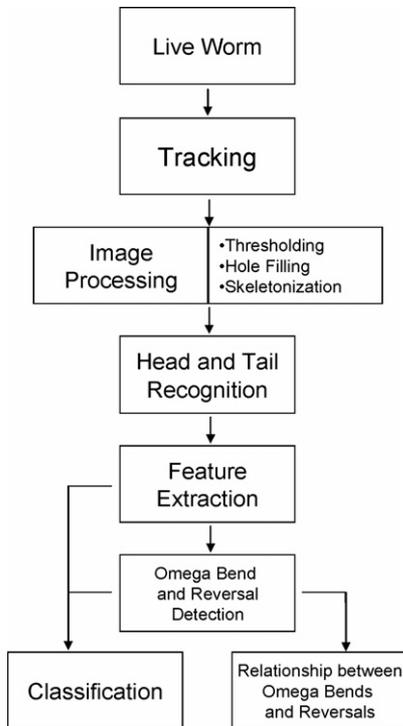
Fig. 2. Block diagram of the data acquisition, image processing and feature steps.

was discarded (Baek et al., 2002; Geng et al., 2003). In this paper, we solved this problem in order to study coiler mutants, which take on these body postures frequently.

A worm body model is used in our algorithm (Fig. 3a). The length L and width W are the average length and width of the worm body obtained from images without internal holes. See Appendix A for details of the algorithm. Briefly, we use W in the model to find the touching parts of the worm body, because touching parts will have width greater than W (Fig. 3b). Then we cut the touching part from its exterior boundary to interior boundary to recover the original posture. The skeletonizing algorithm is then applied to obtain the morphological skeleton. Because *C. elegans* can contract and extend its body, small variations in body length can be accepted as correct skeletons, but with empirical observation, 20% of L was felt to be an upper limit for this variation in body length. If the difference between the obtained skeleton and L is greater than 20% of L, then this
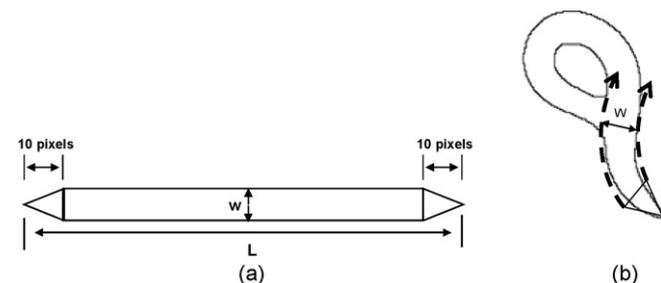

Fig. 3. (a) The worm body matching model. (b) We find the overlapping part of the worm body using the model, by starting from a protruding end and then moving along the body length, looking for a place where the blob width exceeds W.

skeleton is considered erroneous and is not used for further feature extraction and analysis.

2.6. Classification

The Classification and Regression Trees (CART) algorithm is used to analyze features and classify mutant types (Breiman et al., 1984). It is a tree structured statistical analysis and data mining tool. It uses a method known as binary recursive partitioning. During the process, parent nodes are split into exactly two child nodes until the splitting is impossible (only one case in the node) or the desired large tree size is reached. CART first creates large trees and then prunes away branches of the maximal tree, creating a smaller, more efficient tree. Once a tree is complete, CART assigns classes to each terminal node. This is generally done using plurality (the largest percentage of cases in the node).

2.7. Omega bends and reversals

Omega bends occur when the worm takes on the shape of a capital omega; the worm curves its head around to touch the middle part of its body then sharply bends away from its body (Fig. 1c). This posture commonly occurs when the worm makes a large turn with a reorientation of its movement direction greater than 135° (Croll and Smith, 1978). Turns of this sort have been shown to be critical for navigation (or taxis) behaviors used to seek food and other chemoattractants and to avoid toxins and other chemorepellents (Pierce-Shimomura et al., 1999). Different kinds of omega bends also exist for certain worm mutants such as *syd-1(ju82)*, *unc-10(e102)* and *unc-37(e262)*. For *syd-1(ju82)* and *unc-10(e102)*, instead of resembling the Greek letter Ω, the worm's head sometimes touches the middle of the body, then crosses underneath it and goes in another direction. Identifying omega bends is more difficult for *unc-37(e262)* because the movement of this mutant type is jerky or even interrupted by other movements. See Appendix B for the details of our algorithm for detecting omega bends.

In this paper, we use a skeleton based algorithm to detect reversals, as in Feng et al. (2004). Instead of using the distance between the head and the tail, we found it to be more robust to use two points near the two ends as our reference points to decide if the worm was moving forward or backward. In Feng et al. (2004), the angle changing of skewer fits was also used to eliminate certain false positives, but is discarded in our algorithm. A skewer fit is the line segment connecting the head and the tail. See Appendix C for the details of our algorithm for detecting reversals.

3. Results

3.1. Verification of the skeleton algorithm by human observers

The coiling skeletonizing algorithm was tested on fifty-five 5-min videos (8 Hz) from 11 mutant types. Of the 132,000 image frames in these videos, more than 26,000 of them involved body

Table 1a
Verification results for the coiling skeletonizing algorithm

Strain name	Correct skeletons	Wrong skeletons	Wrong skeletons due to vertical body overlapping	Frames rejected by the comparison to the threshold (5000 pixels)
syd-1(ju82)	649 (94.5)	16 (2.3)	22 (3.2)	0
unc-1(e1598)	5178 (99.2)	41 (0.8)	0	0
unc-3(e151)	1705 (93.0)	125 (6.8)	3 (0.2)	0
unc-10(e102)	1690 (90.8)	20 (1.1)	152 (8.2)	0
unc-17(e245)	3245 (82.7)	156 (4.0)	525 (13.3)	3895
unc-26(m2)	3358 (91.4)	79 (2.2)	235 (6.4)	3326
unc-32(e189)	5321 (97.4)	40 (0.7)	104 (1.9)	0
unc-37(e262)	2310 (91.6)	35 (1.4)	176 (7.0)	0
unc-75(e950)	946 (93.6)	37 (3.7)	28 (2.7)	160
unc-77(e625)	1647 (96.1)	20 (1.2)	47 (2.7)	0
Wild type (N2)	189 (99.5)	1 (0.5)	0	0
Total	26238 (93.4)	570 (2.0)	1292 (4.6)	7381

Data were collected from fifty-five 5-min videos (8 Hz) from 11 mutant types. The first column shows the mutant type. The second column shows the number of correct skeletons obtained with our algorithm. The number of wrong skeletons not due to vertical body overlapping is listed in column 3. The number of wrong skeletons due to vertical body overlapping is listed in column 4. The average correct rate is over 93%. Values in parenthesis are in percentage.

touching or overlapping. For all of these, cut images and skeletons were generated by the algorithm for a human observer to verify. The positions of the start and end points of body touching in every cut image were examined. The skeletons were also compared to the grayscale images to decide if the obtained body posture was correct. Experimental results are shown in Table 1a. The rate of obtaining a biologically correct skeleton is over 93%.

Our algorithm for the detection of omega bends was tested on one hundred 5-min videos (8 Hz) in which 303 omega bends were detected by a human observer. The experimental results showed that our algorithm correctly detected over 93% of these 303 omega bends. Also, over 95% of detected events are actually omega bends, so the false positive rate is low even while the true positive rate is high (Table 1b).

Our reversal detection algorithm was tested on the same data set of one hundred 5-min videos (8 Hz) in which 1621 reversal events were detected by a human observer. The experimental results showed that our algorithm can correctly detect reversals at a high rate (96.9%) that compared favorably with that of the previously described (Feng et al., 2004) skeleton based algorithm (86.3%). This higher correct detection rate was furthermore accompanied by a lower rate of false alarms (only 10

Table 1b
Verification results for the omega bend detection algorithm

Strain name	No. of detected omega bends	No. of wrong detections	No. of omega bends missed
Wild type (N2)	57 (100)	0	7
syd-1(ju82)	43 (100)	0	0
unc-10(e102)	41 (97.6)	1	3
unc-37(e262)	83 (91.2)	8	0
unc-75(e950)	60 (92.3)	5	9
Total	284 (95.3)	14	19

Data were collected from one hundred 5-min videos (8 Hz) from five mutant types. The first column shows the mutant type. The second column shows both the number of correctly detected omega bends with our algorithm and the associated positive predictive value (PPV). The PPV is the ratio of correct detections to total detections. The number of wrong detections is listed in column 3. The number of missed omega bends is listed in column 4. Values in parenthesis are in percentage.

wrong detections compared to 14 for the previous algorithm). We applied the reversal detection algorithm described in Feng et al. (2004) to our data set of one hundred 5-min videos with 1621 reversal events so the results are directly comparable (Table 1c).

Table 1c
Verification results for the reversal detection algorithm

Strain name	Our algorithm			Algorithm from Feng et al. (2004)		
	No. of reversals detected	No. of wrong detections	No. of reversals missed	No. of reversals detected	No. of wrong detections	No. of reversals missed
Wild type (N2)	494 (100)	0	0	473 (100)	0	21
syd-1(ju82)	342 (99.4)	2	12	334 (99.4)	2	20
unc-10(e102)	262 (99.6)	1	3	252 (97.7)	6	13
unc-37(e262)	105 (96.3)	4	13	87 (94.6)	5	31
unc-75(e950)	368 (99.2)	3	22	303 (99.7)	1	87
Total	1571 (99.4)	10	50	1399 (99.0)	14	172

Data were collected from one hundred 5-min videos (8 Hz) from five mutant types. The first column shows the mutant type. The first column shows the mutant type. The second column shows both the number of correctly detected reversals with our algorithm and the associated positive predictive value (PPV). The PPV is the ratio of correct detections to total detections. The number of wrong detections is listed in column 3. The number of missed reversals is listed in column 4. Values in parenthesis are in percentage.

Table 2
Description of uncoordinated mutants (WormBase website, http://www.wormbase.org; Hodgkin, 1983)

unc-1	Strong coilers
unc-3	Weak coiler tends to coil tail active
unc-10	Weak coiler tends to back loopy movement in reverse; fairly active slightly small and thin
unc-17	Severe coiler at all stages rather small and thin
unc-26	Severe kinker small scrawny flaccid little movement
unc-32	Severe coiler little movement in adult; moves well in L1 but coils in response to touch in L2 and later stages; rather small and thin
unc-37	Weak coiler fairly active
unc-75	Weak coiler especially in reverse; moves forward well; sluggish; short
unc-77	Irregular loopy movement both forward and reverse; active; thin

3.2. Assessment of skeleton algorithm by classification of coiler mutants

To evaluate the effectiveness of our system in characterizing the postures of coiled animals, we tested the ability of the automated binary classifier CART to correctly identify different mutant strains that frequently adopt coiled postures. We compared our data from 10 different uncoordinated mutants with wild-type worms.

The test group included five mutants categorized by Hodgkin (1983) as "weak coilers" (*unc-3*, *unc-10*, *unc-37*, *unc-75* and *unc-77*) as well as two "strong coilers" (*unc-17* and *unc-32*), one "forward uncoordinated" mutant (*unc-1*), one "strong kinker" (*unc-26*) and one mutant with superficially normal locomotion (*syd-1*). Table 2 contains detailed descriptions of behaviors of these mutants. The data set contained forty 5-min videos at 8 Hz

of each mutant type. Shown in Fig. 4, a classification tree with 11 terminal nodes (depicted as ellipses) was generated by CART using 10-fold cross-validation to determine the tree size. Only nine different features, appearing in diamond-shaped boxes in Fig. 4, were chosen by CART and used as splitting nodes in this classification tree. The names and descriptions of these nine features were as follows: ANCHSMAX—maximum value of angle change rate; AVEBRMIN—minimum value of worm average brightness; CNTMVAVG—average value of centroid movement distance; HAREAMIN—minimum value of head area; HDTLRMAX—minimum value of head thickness–length ratio; HTTHRMAX—minimum value of head–tail thickness ratio; LNGTHMIN—minimum value of worm body length; TAREAMIN—minimum value of worm tail area; TLCTDAVG—average value of tail–centroid distance. This subset of features selected from among the 188 features to be
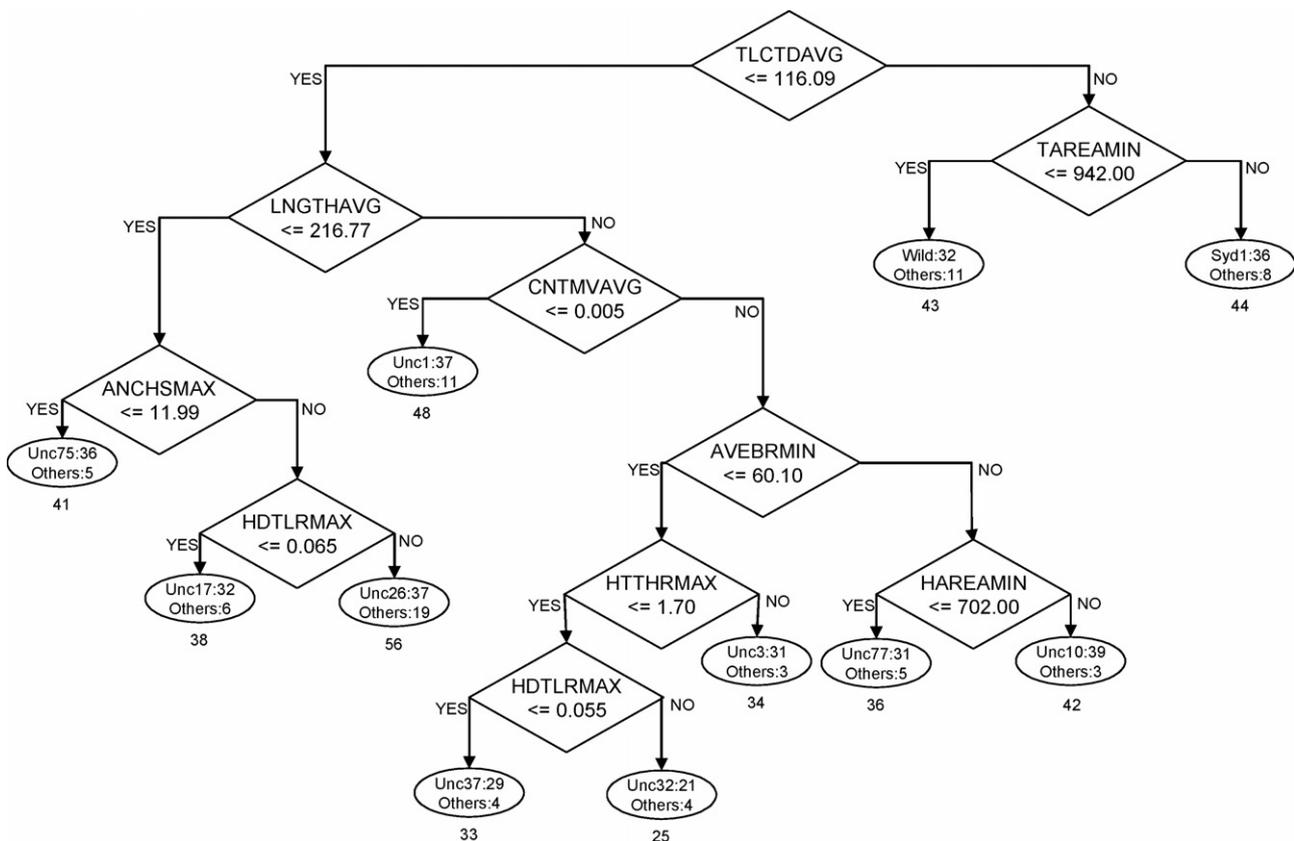

Fig. 4. The classification tree reliably identifies the type of a given worm using only nine features. The tree was constructed using the CART algorithm as described.

used as the basis for splitting, as well as the thresholds used for splitting, were chosen automatically by the CART algorithm based on the data, with the cross-validation used to guard against overfitting. At each step, a splitting test separates a parent node into exactly two child nodes based on a criterion related to a single feature. For example, suppose we have a worm of unknown type with TLCTDAVG = 113.82, LNGTHAVG = 193.43 and ANCHSMAX = 11.72. Starting at the top, the first question is:

$$\text{Is TLCTDAVG} \leq 116.09?$$

In this case, the answer is *yes* and the case goes to the left. This classification tree will do the same for LNGTHAVG and then ANCHSMAX and the worm winds up in the ellipse on the left and is classified as *unc-75*. The classification result shows the significance of previously generated skeletons. Several of the features such as angle change rate, body length as well as head–tail recognition rely on measurements of the skeleton.

The cross-validated classification probabilities for the system with the new algorithm compared to the standard morphological skeleton algorithm are given in Table 3A and B, respectively. The mutant names of all video data are in the first column and the first row lists the groups to which each video was classified. The success rates are listed along the diagonal while the off-diagonal entries represent the misclassification rates. We see that the CART tree using the data from the new skeletonizing algorithm has significant improvement for several mutants. For example, the correct classification rate for *syd-1* improves by 12.5%, *unc-10* by 20%, *unc-37* by 10% and *unc-77* by 12.5%.

There are a few minor changes as well: *unc-3* gets worse by 5%, and *unc-17* and *unc-32* each improve by 2.5%. Overall, the new skeletonizing algorithm does allow us to do better classification for the given video data. Given that the old system already showed better success at correctly classifying difficult-to-distinguish mutant types than a human expert (Geng et al., 2004), we consider this to be a good result.

3.3. Analysis of omega bends and reversals

In another experiment, we used our system to compare omega bend and reversal behavior of mutant and wild-type animals. In particular, we investigated the temporal correlation between these body movements, since omega bends have recently been observed to frequently follow reversals (Gray et al., 2005). We focused on those mutants in our data set, *syd-1*, *unc-10*, *unc-37*, *unc-75* and *unc-77*, which are described as "fairly active" in the literature. Our reversal and omega bend detection algorithms were used on all video data of these five mutants and wild type. For each omega bend event in each video, we searched for the closest reversal happening within 5 s before the omega bend event. If no reversal occurred within 5 s, the omega bend event was considered to have not followed a reversal. We also calculated the average time interval between pairs of reversals and omega bends in each mutant type, as well as whether the omega bend involved contraction of the dorsal or ventral body muscles. The results are shown in Table 4.

We observed that in wild type as well as *syd-1* mutant animals, omega bends showed a distinct ventral bias. In fact, for omega

Table 3
The cross-validated classification probability tables from two systems

	syd-1	unc-1	unc-3	unc-10	unc-17	unc-26	unc-32	unc-37	unc-75	unc-77	Wild type (N2)
(A) Results with new skeletonizing algorithm (%)											
syd-1	**80.0**	0	0	2.5	0	0	0	2.5	0	0	15.0
unc-1	5.0	**85.0**	0	0	0	2.5	2.5	0	0	0	5.0
unc-3	5.0	7.5	**67.5**	0	0	0	10.0	7.5	2.5	0	0
unc-10	0	2.5	0	**92.5**	0	0	0	0	0	2.5	2.5
unc-17	0	0	0	0	**77.5**	10.0	5.0	0	0	5.0	2.5
unc-26	0	0	0	0	22.5	**72.5**	0	0	5.0	0	0
unc-32	0	12.5	0	0	7.5	2.5	**57.5**	10.0	5.0	5.0	0
unc-37	5.0	0	7.5	0	0	2.5	10.0	**67.5**	0	2.5	5.0
unc-75	0	2.5	0	0	7.5	0	2.5	0	**87.5**	0	0
unc-77	0	7.5	5.0	12.5	10.0	0	0	2.5	0	**62.5**	0
Wild type (N2)	25.0	5.0	0	0	0	0	0	0	0	2.5	**67.5**
(B) Results with previous system (Geng et al., 2004) (%)											
syd-1	**67.5**	0	0	5.0	0	0	2.5	2.5	0	0	22.5
unc-1	5.0	**85.0**	0	0	0	2.5	2.5	0	0	0	5.0
unc-3	5.0	7.5	**72.5**	0	0	0	7.5	0	2.5	2.5	2.5
unc-10	0	0	5.0	**72.5**	0	0	15.0	0	0	5.0	2.5
unc-17	2.5	0	0	0	**75.0**	12.5	5.0	2.5	0	2.5	0
unc-26	0	0	0	0	20.0	**72.5**	2.5	0	5.0	0	0
unc-32	0	10.0	0	12.5	5.0	2.5	**55.0**	7.5	5.0	2.5	0
unc-37	0	0	10.0	5.0	0	2.5	12.5	**57.5**	0	7.5	5.0
unc-75	0	2.5	0	0	7.5	0	2.5	0	**87.5**	0	0
unc-77	0	7.5	5.0	10.0	10.0	0	0	17.5	0	**50.0**	0
Wild type (N2)	22.5	5.0	0	2.5	0	0	0	0	0	2.5	**67.5**

In each table, the first column lists the actual mutant types for the video data. The first row lists the results of the classification procedure. The success rates are listed along the main diagonal (bold values) while the off-diagonal entries represent the misclassification rates.

Table 4
Relationship between omega bends and reversals

	Wild type (N2)	*syd-1(ju82)*	*unc-10(e102)*	*unc-37(e262)*	*unc-75(e950)*	*unc-77(e625)*
No. of videos watched	56	81	40	68	40	40
No. of omega bends following reversal (total)	75 (0.43)	111 (1.01)	74 (1.26)	45 (1.83)	37 (2.88)	71 (0.75)
No. of omega bends following reversal (ventral)	75 (0.43)	98 (0.86)	58 (1.10)	22 (1.90)	16 (3.05)	47 (0.67)
No. of omega bends following reversal (dorsal)	0	13 (2.16)	16 (1.84)	23 (1.76)	21 (2.74)	24 (0.92)
No. of omega bends NOT following reversal (total)	3	9	20	147	58	48
No. of omega bends NOT following reversal (ventral)	2	5	11	103	16	28
No. of omega bends NOT following reversal (dorsal)	1	4	9	44	42	20

Average time intervals (s) between pairs of reversals and omega bends are listed in parenthesis.

bends that immediately followed a reversal, nearly all involved a bend on the ventral side of the body. *unc-10* and *unc-77* mutants also have a statistically significant ventral bias (p-value 0.0000057 and 0.0045 for *unc-10* and *unc-77*, respectively, using a Chi-Square test) (Glantz, 1996). However, the ventral bias is less strong for these mutants than for wild type (p-value ≈ 0). However, for *unc-37* and *unc-75* mutants, dorsal bends were as common as ventral bends, indicating that the ventral bias was lost in these animals. Furthermore, these mutants also showed a much higher frequency of omega bends that were uncorrelated with reversals, and the average time interval between omega bends and reversals was significantly increased. Thus, the *unc-37* and *unc-75* mutants appeared to have abnormalities in both the ventral bias of omega bends as well as their temporal correlation with reversals. Since we looked at single alleles of these mutants, it is not possible to conclude definitively that the ventral bias phenotype is due to the *unc-37/unc-75* mutation rather than another mutation in the genetic background. However, these results demonstrate that it is possible to detect such phenotypes (which would be extremely tedious and time-consuming for a human observer) using the automated system.

In summary, we confirmed the loss of temporal correlation between reversals and turns in some but not all uncoordinated mutants, and demonstrated the possibility of using our automated system to identify other correlations in the timing of behavioral events that would be difficult to discern through real-time observation.

4. Discussion

We have shown that a biologically meaningful morphological skeleton can be obtained with our coiling skeletonizing algorithm for a worm body shape having an internal hole. This represents an important advance in the automated analysis of nematode behavior, particularly with respect to the study of certain classes of locomotion-abnormal mutants. Whereas wild-type nematodes, and animals with locomotion patterns close to wild type, coil infrequently, for coiler mutants a significant proportion of frames in a given video sequence will contain internal-hole images.

Moreover, we have demonstrated that locomotion features extracted from obtained skeletons can be used to classify coilers with highly similar phenotypes. Among the coilers we studied, *unc-3*, *unc-10*, *unc-37*, *unc-75* and *unc-77* are all described as

weak coilers; *unc-1*, *unc-17*, *unc-26* and *unc-32* are described as strong coilers or kinkers. Yet each of these types could be distinguished from others in its described class by a classifier using the features extracted by our system. For example, from our classification tree (Fig. 4), we can see that *unc-75* is the shortest within weak coilers, and has smaller values of length-related features (body length and tail–centroid distance). *unc-10* is the largest weak coiler and it has longer length and larger body area. For strong coilers, *unc-32* is the longest and *unc-1* showed particularly low centroid movement. *unc-26*, which has larger head width–length ratio, tends to have a fatter head when compared to *unc-17* (where fatness is defined as the ratio of worm area to length). *syd-1* does not coil very often and moves very smoothly, similar to wild type in previous human observation. We found that it also has length very similar to wild type. The most significant difference between *syd-1* and wild type is that *syd-1* has larger tail area than wild type. Note that worm head/tail identification is performed, as in Geng et al. (2004), using the facts that the worm's head moves more frequently than the tail, and is darker than the tail.

The relationships between omega bends and reversals for six strains (wild type, *syd-1*, *unc-10*, *unc-37*, *unc-75* and *unc-77*) were also examined and compared to each other in this paper. Using our automated omega bends and reversal detection algorithms, we found that the ventral bias of omega bends normally observed in wild type was largely absent in some mutants such as *unc-37* and *unc-75*. Likewise, the temporal correlation between omega bends and reversals was defective for these two strains. Wild type, *syd-1*, *unc-10* and *unc-77* have very similar omega bend and reversal behaviors. The ventral bias is very strong particularly in wild type and *syd-1*, and most detected omega bends were tightly coupled temporally to reversals for these four strains.

5. Conclusion

In comparison with related studies (Geng et al., 2003, 2004; Feng et al., 2004), the six contributions of the current work can be summarized as follows: (1) We developed and tested a new algorithm for obtaining correct morphological skeletons from worm body shapes that have internal holes. (2) In comparison with previous skeletonization algorithms (which abandoned frames with internal holes) the new algorithm increases classification correctness for several coiler mutant types (which frequently

take on body postures with internal holes). (3) We provided quantitative characterizations of several coiler mutants. (4) We developed and tested an algorithm for automatic detection of omega bends, which correctly detected 93% of the omega bend events. (5) We developed and tested an algorithm for automatic detection of reversals, which correctly found 96.9% of reversal events, compared to the 86.3% identification rate of Feng et al. (2004), while having fewer false alarms. (6) We found that both the ventral bias of omega bends normally observed in wild type, as well as the temporal correlation between omega bends and reversals, were largely absent in some coiler mutants such as *unc-37* and *unc-75*.

In previous studies, coiling frames were disregarded for all the 127 skeleton-related features derived from morphological skeleton parameters. These new methods make it possible for the first time to obtain skeleton parameters from virtually all images. Complex behavioral features such as reversals and omega bends have been shown to reveal important aspects of sensory perception and motor control in the *C. elegans* nervous system; however, manual scoring of these features is tedious and labor-intensive. The development of automated methods for the study of complex behavioral patterns and the identification of mutants with abnormalities in them promises significantly to enhance the understanding of behavioral mechanisms in this important neurobiological model.

Appendix A. Coiling skeletonizing

Images with holes can be classified into three groups: (A) images with the worm body touching only in the horizontal (*xy*-plane) direction and having a protruding head/tail (Fig. 1d), (B) images with the worm body touching only in the horizontal direction but not having any protruding head/tail (Fig. 1e) and (C) images with the worm body overlapping vertically that is, in the *z*-direction, going out of the plane of the agar plate. For images in group C, because the worm covers part of its body with another part, its body area is smaller than its usual size. For every binarized image, we compare the size of the worm body area to a threshold. The threshold is recommended to be 90% of the average worm body area. Among the mutants studied in this paper, *unc-17*, *unc-26* and *unc-32*, which have smaller body areas (5500 pixels) than the other strains, were strong coilers/kinkers. Only these strains have the possibility of coiling
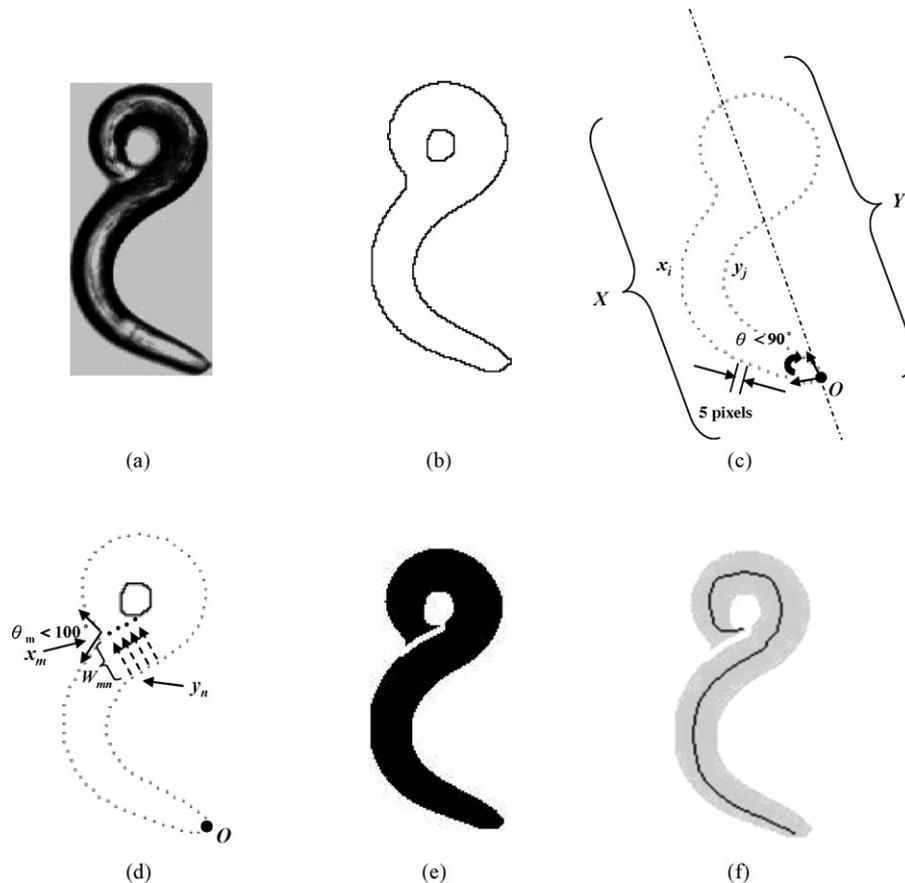

Fig. A.1. An example of coiling skeletonizing for group A (case 1). (a) The original grayscale image. (b) The exterior and interior boundaries. (c) Sampled boundary and two sets X and Y. (d) Finding the starting point and generating the division line. (e) The cut image. (f) The morphological skeleton (solid line) obtained from the cut image.

so tightly that the skeletonization should be directly abandoned (images in group C). So we chose 5000 pixels as the threshold in our experiment, but this threshold could be chosen as 90% of the average worm body area if either a different magnification were used, or if strong coilers with different body sizes were studied. If the body area is smaller than the threshold, we decide the image is in group C and abandon it because the correct body posture will not be available when a worm has vertical overlapping.

For images in groups A and B, after the binarization of the original grayscale image, we obtain the exterior boundary and the interior boundary of the worm body by first eroding it with a 3×3 square structuring element and then performing the set difference between the binary image and its erosion. Figs. A.1a and A.2a show the grayscale original images of two cases that will ultimately be classified as belonging to class A. Figs. A.1b and A.2b depict the corresponding exterior and interior boundaries. Fig. A.3a shows the grayscale original image of a case that will be classified as class B. Fig. A.3b shows the exterior and interior boundaries. In each case, these two boundaries are sampled at an interval of 5 pixels (the sampling interval should be adjusted according to the magnification used for data acquisition) to get $N+1$ sampled points p_i ($i = 0, 1, 2, 3, \ldots, N$, where $N+1$ is the total number of sampled points). To decide if this image has a protruding head/tail, the inner angle θ between each pair of

segments p_i–p_{i-2} and p_i–p_{i+2} in the exterior boundary will be measured to find a point O which has the furthest distance from the interior boundary among all points with $\theta < 90°$. If no such point exists, then this image is classified as group B. Otherwise, this image belongs to group A. In Figs. A.1c and A.2c, the point O is found and the images are classified as class A. In Fig. A.3c, there is no point where the interior angle is less than $90°$, so the image is class B (no protruding head/tail).

If this image is in group A, all sampled points are divided into two sets: set X contains $N/2$ points clockwise next to point O and set Y contains $N/2$ points counterclockwise next to point O. For each point x_i in X, we search every point y_j in Y to find the one closest to x_i. We calculate the distance W_{ij} between x_i and y_j as well as the outer angle θ_i (the angle between each pair of segments x_i–x_{i-2} and x_i–x_{i+2}). First we check for all points if $\theta_i < 100°$, if the answer is *yes*, then x_i is considered a possible starting point of the worm body touching. If the answer is *no* for all points, we compare W_{ij} to the average width W of the worm body. If $W_{ij} > W$, then x_i will still be considered a possible starting point. The search continues until the first possible starting point of the body touching is found. We repeat the same process for the set Y. We have found that at most one set will have a possible starting point with θ smaller than $100°$ (Fig. A.1d). Sometimes neither set X nor Y has an outer angle θ smaller than $100°$. In this
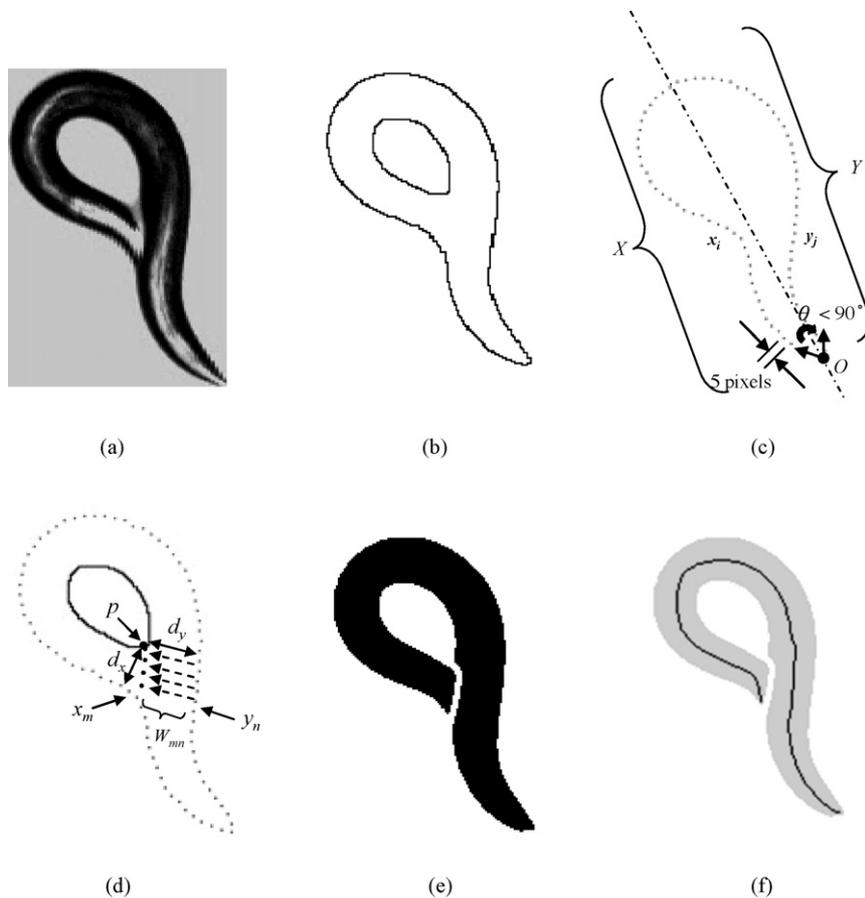

Fig. A.2. An example of coiling skeletonizing for group A (case 2). (a) The original grayscale image. (b) The exterior and interior boundaries. (c) Sampled boundary and two sets X and Y. (d) Finding the starting point and generating the division line. (e) The cut image. (f) The morphological skeleton (solid line) obtained from the cut image.
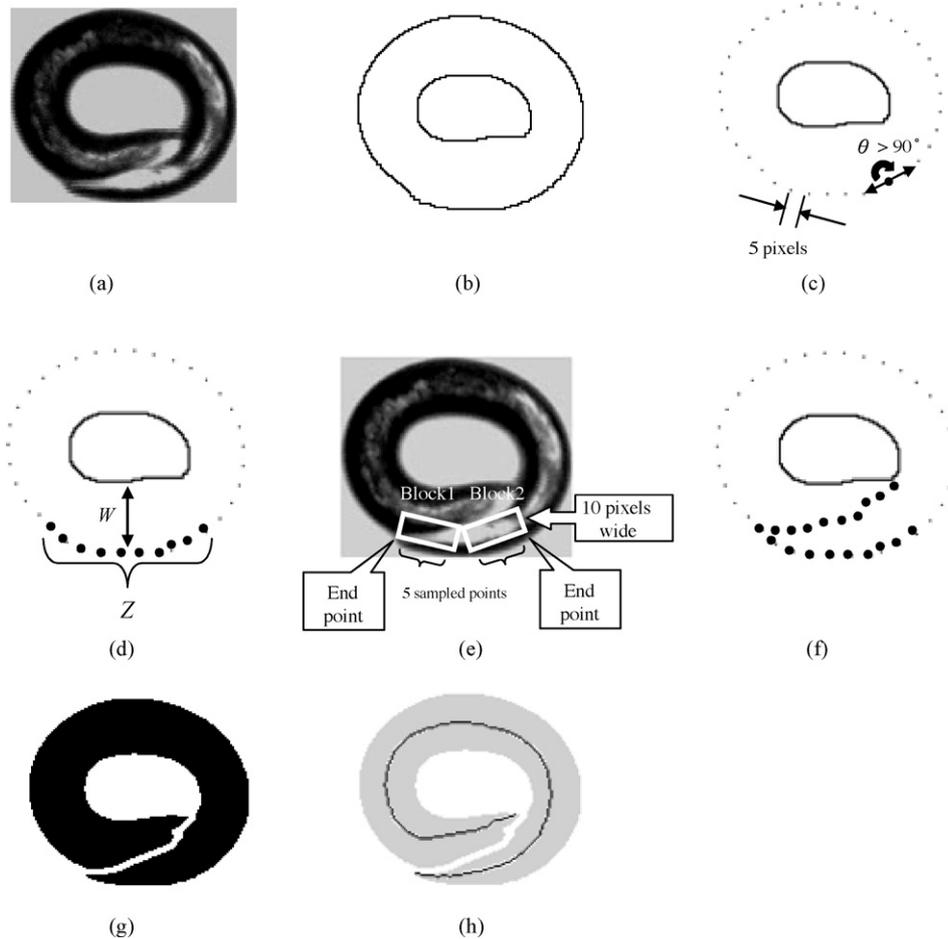
Fig. A.3. An example of coiling skeletonizing for group B. (a) The original grayscale image. (b) The exterior and interior boundaries. (c) sampled boundary. There is no point where the angle is less than 90°. (d) Finding overlapping part. (e) Comparing variance of pixel values in two areas. (f) Locate division points from the starting point to the interior boundary. (g) The cut image with the division line. (h) The morphological skeleton (solid line) obtained from the cut image.

case, both sets X and Y will have a possible starting point where $W_{ij} > W$. We find a point p in the interior boundary which is the closest to the two possible starting points found, then we compare d_x and d_y which are the shortest distances from the point p to sets X and Y. Whichever side has the shorter distance will be considered the head/tail part (because the head and tail are less thick) and the possible starting point in that side will be considered the real starting point of the worm body touching (Fig. A.2d).

Assume x_m is found to be the real starting point and y_n is its closest sampled point in the other set, we can keep locating division points which are W_{mn} (the distance between x_m and y_n) pixels away from the next points y_k ($k > n$) until the interior boundary is reached. These division points are connected to form a division line and then a skeletonizing algorithm is applied on this cut image (Figs. A.1e and A.2e) to get the correct skeleton (Figs. A.1f and A.2f).

If the image is in group B, we calculate the distance d between the interior boundary and every sampled point on the exterior boundary. If $d > W$, we put this point into a set Z. The set Z covers the overlapping part of the worm body (Fig. A.3d). The two end points of this set are the two possible starting points of the overlapping. We measure the variance of pixel values in two rectangular blocks (each block has 10-pixel width with one of the

longer edges formed by one end point and the fifth point from the end point. The size of the rectangular blocks should be adjusted according to the magnification used) around these two points and compare them (Fig. A.3e). The side with larger variance is considered the starting point because the place where the head or tail tapers to a point usually has very different pixel values compared to the body part it is touching. The histograms of two rectangular blocks are shown in Fig. A.4. A number of points are located gradually from the starting point with increasing distance (0, 2, 4, 6, …, W) from points in the set Z until the interior boundary is reached (Fig. A.3f) and connected together to generate a division line (Fig. A.3g). Then we apply a standard skeletonizing algorithm on this cut image to obtain the correct skeleton of the worm body (Fig. A.3h). The block diagram of the whole coiling skeletonizing process is also shown in Fig. A.5.

Every skeleton obtained with this algorithm was also compared to the average length of the worm body calculated from images without internal holes. If the difference between them is greater than 20% of the average worm body length, which is nearly the difference between the maximal and the minimal worm body length in frames without body touching, then this skeleton is assumed to be incorrect and is not used for further feature extraction.
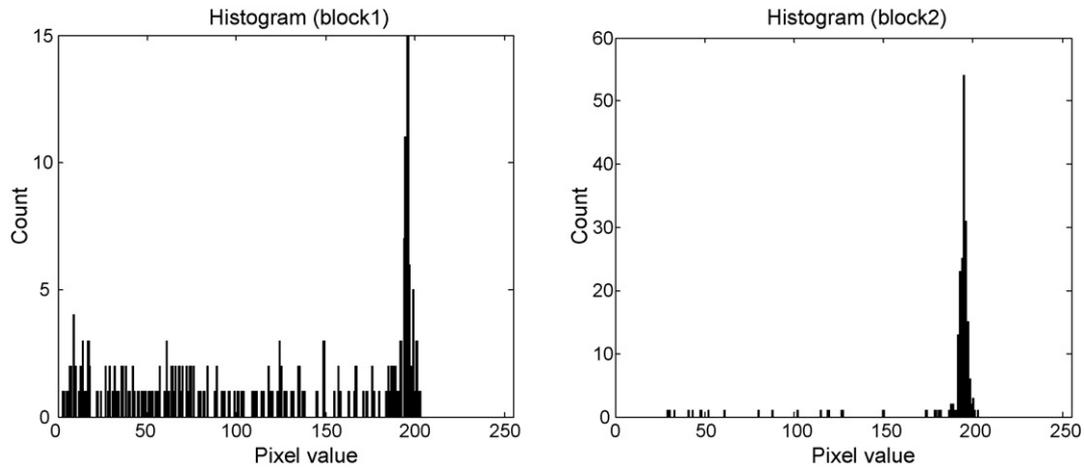
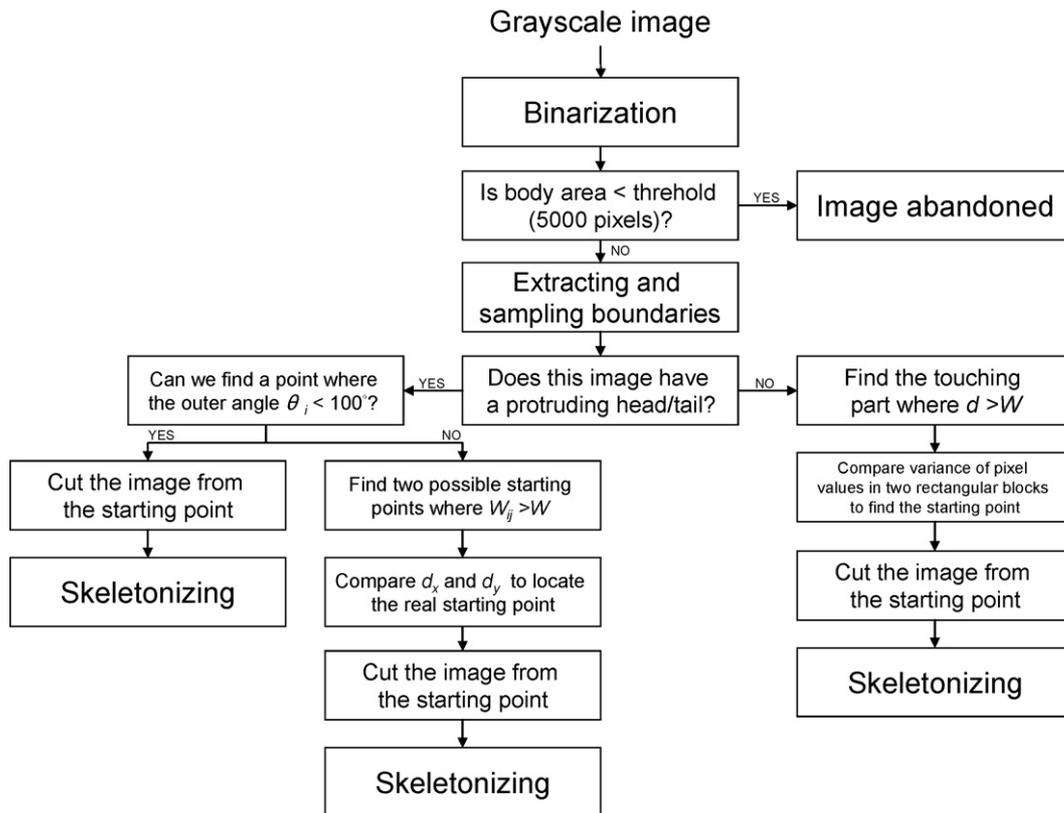Fig. A.4. The histograms of block 1 and block 2 in Fig. A.3e.

Fig. A.5. The block diagram of coiling skeletonizing algorithm.

Appendix B. Omega bend detection

A typical omega bend starts with the worm making a big turn by approaching its body with its head, then its head will pass its tail and go to a new direction. As defined in Gray et al. (2005), the reorientation has to be greater than 135° or the worm has to touch its body in order for the movement to be considered an omega bend. For coiler mutant types, sometimes an omega bend is interrupted by other movements before it is finished. Our goal is to construct an algorithm which can automatically detect complete omega bend events that meet the definition as given in

Gray et al. (2005). In our algorithm, we divide an omega bend into three parts:

(1) Start of an omega bend:

For each frame, we compare the distance d_{hm} (the distance between the worm head and the middle skeleton point which is defined as the 15th skeleton point) and the distance d_{tm} (the distance between the worm tail and the middle skeleton point) and calculate the angle θ between these two segments. We use L to denote the worm's body length. If $d_{hm} < d_{tm} - 0.05L$ and $\theta < 45°$, then this frame
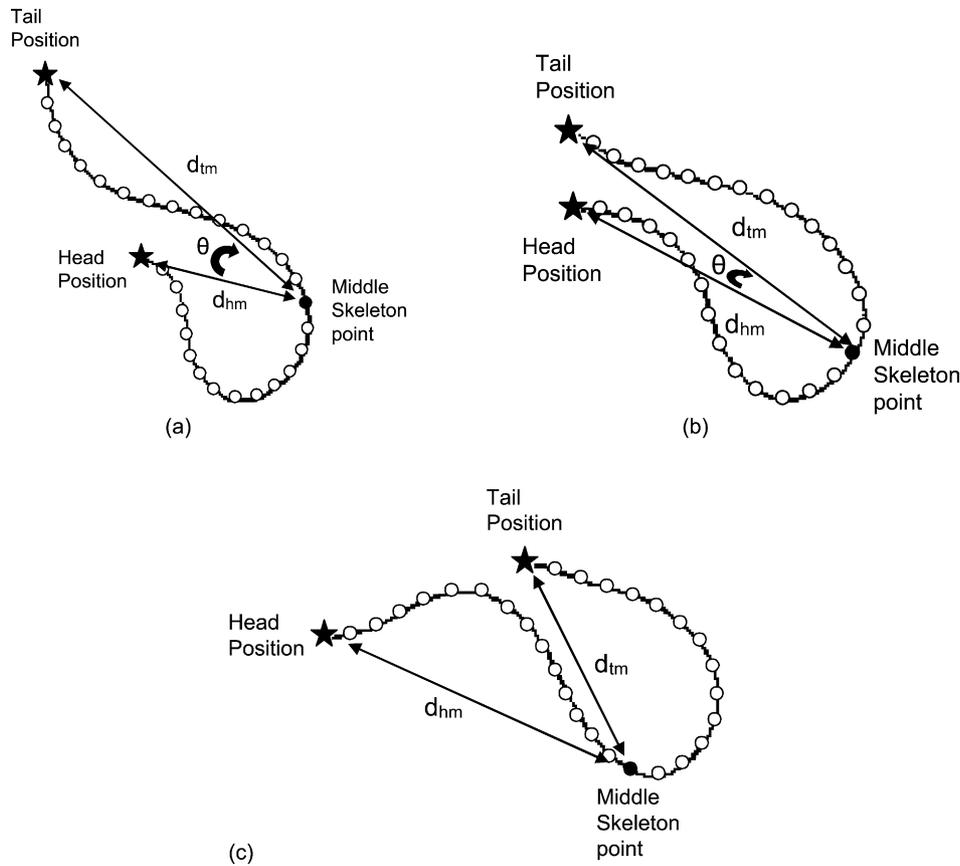
Fig. B.1. (a) Start frame of an omega bend. Segment d_{tm} must be greater than d_{hm} plus 5% of body length and θ must be less than 45°. (b) A frame during an omega bend. θ must be less than 45°. (c) End frame of an omega bend. Segment d_{hm} must be greater than d_{tm} plus 5% of body length.

will be considered a starting frame of an omega bend (Fig. B.1a).

(2) Middle of an omega bend:

Because the reorientation of an omega bend has to be greater than 135°, the angle θ (same definition as in start of an omega bend) has to be smaller than 45° in all frames of an omega bend (Fig. B.1b). Sometimes a worm touches itself during an omega bend. In all frames with touching, the bending angle θ is obviously smaller than 45° (close to 0), so these frames also satisfy the criterion of the middle of an omega bend.

(3) End of an omega bend:

When a worm comes out of an omega bend, its head moves away from its body to a new direction.

At this moment, its tail should be closer to its middle skeleton point then its head. So $d_{tm} < d_{hm} - 0.05L$ in the end of the omega bend (Fig. B.1c).

If the first frame, the last frame and all frames in the middle of a sequence satisfy these criteria of start, end and middle of an omega bend, we declare an omega bend.

Appendix C. Reversal detection

After a morphological skeleton is obtained, 30 evenly spaced skeleton points are extracted. The two end points on the skeleton represent the head and tail positions. Two reference points (R_h, R_t) are defined as the sixth skeleton point from the head and tail end points (Fig. C.1a). These mark where the tail segment and head segment begin.

Any frame without body looping (that is, without an internal hole) will be considered a reversal frame if the following criteria are satisfied:

(1) The distance between the head position four frames earlier ($t = n - 4$) and the current reference point R_h ($t = n$) has to be greater than the distance between the current head position ($t = n$) and the current reference point R_h ($t = n$). When this criterion is satisfied, it means that the worm's head is moving toward its previous body position.

(2) The distance between the current tail position ($t = n$) and the previous reference point R_t ($t = n - 4$) has to be greater than the distance between the previous tail position ($t = n - 4$) and the previous reference point R_t ($t = n - 4$) by at least 2.0% of the body length (Fig. C.1b).

When the second criterion is satisfied, it means that the worm's tail is moving away from its previous body position. It will exclude those frames in which the worm only waves its tail instead of reversing. The "2.0% of the body length" in the second criterion makes the reversal length showing on the computer long enough (≥ 1 mm) to be verified by human observation. The
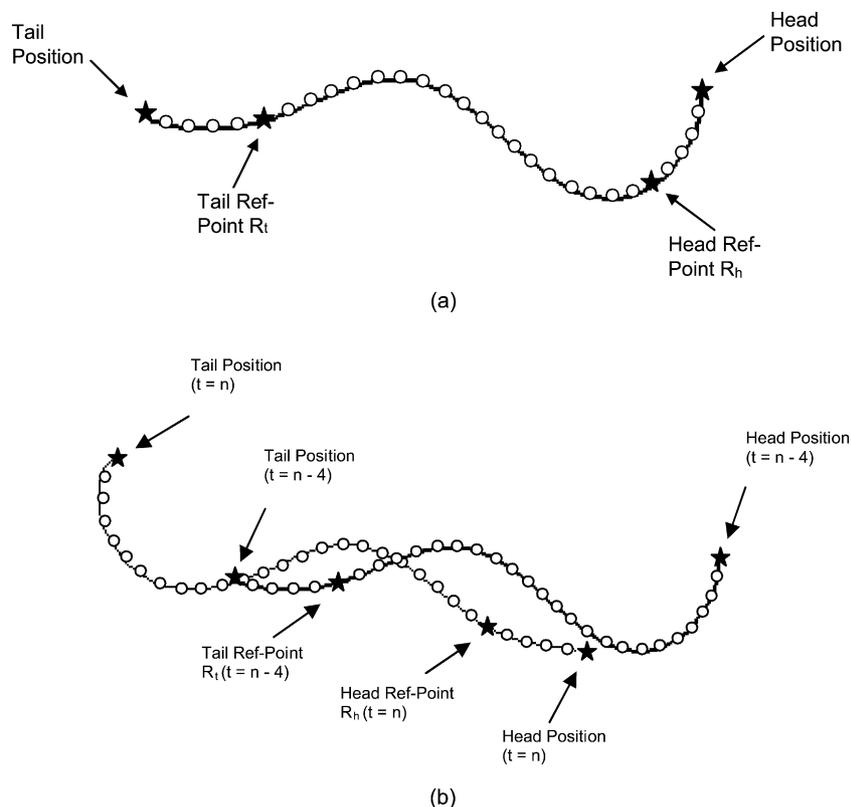
Fig. C.1. (a) Skeleton with 30 sampled skeleton points. Two reference points are defined as the sixth skeleton points from two end points (head position and tail position). (b) Reversals detection method. The frame at $t = n$ is compared to the earlier frame at $t = n - 4$.

reason we chose to compare the frames at n and $n - 4$ (instead of $n - 1$) is to make our result less sensitive to other movements besides reversals such as tiny tail waving or head foraging movements.

After the reversal frames are found, we combine them to locate every reversal sequence happening during the video. The reversal distance and length are obtained by calculating the moving distance of the centroid and the time interval between the start frame and the end frame of a reversal sequence.

References

Baek J, Cosman P, Feng Z, Silver J, Schafer WR. Using machine vision to analyze and classify *Caenorhabditis elegans* behavioral phenotypes quantitatively. J Neurosci Meth 2002;1(18):9–21.

Breiman L, Friedman J, Olshen R, Stone C. Classification and Regression Trees. Belmont, CA: Wadsworth; 1984.

Brenner S. The genetics of *Caenorhabditis elegans*. Genetics 1974;77: 71–94.

Croll NA, Smith JM. Indolealkylamines in the coordination of nematode behavioral activities. Can J Zool 1975;53:894–903.

Croll NA, Smith JM. Integrated behaviour in the feeding phase of *Caenorhabditis elegans* (Nematoda). J Zool Lond 1978;184:507–17.

Cronin CJ, Mendel JE, Mukhtar S, Kim YM, Stirbl RC, Bruck J, et al. An automated system for measuring parameters of nematode sinusoidal movement. BMC Genet 2005;6:5.

Feng Z, Cronin CJ, Wittig Jr JH, Sternberg PW, Schafer WR. An imaging system for standardized quantitative analysis of *C. elegans* behavior. BMC Bioinform 2004;5:115.

Geng W, Cosman P, Baek J, Berry C, Schafer WR. Quantitative classification and natural clustering of *Caenorhabditis elegans* behavioral phenotypes. Genetics 2003;165:1117–26.

Geng W, Cosman P, Berry C, Feng Z, Schafer WR. Automatic tracking, feature extraction and classification of *C. elegans* phenotypes. IEEE Trans Biomed Eng 2004;51:1811–20.

Glantz AS. Primer of biostatistics. 4th ed. McGraw-Hill; 1996.

Gonzalez R, Woods R. Digital image processing. 2nd ed. NJ: Prentice Hall; 2002.

Gray JM, Hill JJ, Bargmann CI. A circuit for navigation in *Caenorhabditis elegans*. Proc Natl Acad Sci USA 2005;102:3184–91.

Hardaker LA, Singer E, Kerr R, Zhou GT, Schafer WR. Serotonin modulates locomotory behavior and coordinates egg-laying and movement in *Caenorhabditis elegans*. J Neurobiol 2001;49:304–11.

Hodgkin J. Male phenotypes and mating efficiency in *Caenorhabditis elegans*. Genetics 1983;103:43–64.

Jain R, Rangachar K, Schunck B. Machine vision. NY: McGraw-Hill; 1995.

Pierce-Shimomura J, Morse TM, Lockery SR. The fundamental role of pirouettes in *Caenorhabditis elegans* chemotaxis. J Neurosci 1999;19:9557–69.

Rankin CH, Chiba C, Beck C. *Caenorhabditis elegans*: a new model system for the study of learning and memory. Behav Brain Res 1990;37:89–92.

Wicks SR, Rankin CH. Integration of mechanosensory stimuli in *Caenorhabditis elegans*. J Neurosci 1995;15:2434–44.

Zheng Y, Brockie PJ, Mellem JE, Madsen DM, Maricq AV. Neuronal control of locomotion in *C. elegans* is modified by a dominant mutation in the GLR-1 ionotropic glutamate receptor. Neuron 1999;24:347–61.